

# no red Antenna calibration and foreground modeling errors in 21-cm Global experiments

Christos I. Kolitsidas,<sup>1\*</sup> and Eloy de Lera Acedo<sup>2</sup>

<sup>1</sup>*KTH Royal Institute of Technology, Stockholm, SE-10044 Sweden*

<sup>2</sup>*Cavendish Laboratory, University of Cambridge, Cambridge, CB3 0HE, United Kingdom*

Accepted XXX. Received YYY; in original form ZZZ

## ABSTRACT

The change in the energy state of neutral hydrogen atoms results in electromagnetic radiation that corresponds to approximately 21 cm wavelength in free space and can act as a probe to cosmological observations. The remaining redshifted 21-cm signal from the epoch of reionization - EoR is buried under a much brighter (several orders of magnitude) foreground radiation. The aim of this work is to investigate the residual errors of using different foreground models as well as antenna beam model uncertainties based on known measurement errors. The residual errors are defined as the  $\ell^2$ -norm of the difference between a calculated quantity and its polynomial fitted approximation. Filtering strategies of the measurement uncertainties are also explored. Our analysis is based on four different, realistic antenna models and an ideal dipole antenna over an infinite ground plane, that serves as a reference case. For realistic antenna models, we have utilized a single reflector antenna based on the Hydrogen Epoch of Reionization Array - HERA; a single log-periodic antenna based on that used by the Square Kilometre Array - SKA Low telescope SKALA; a wideband, widescan angle Capacitively Loaded Dipole Array - CLDA and a dipole antenna. The choice of these models is because they are representative of different antenna classes of possible candidates for a global EoR experimental set-ups. Utilizing physically realistic foreground and antenna models we present the residual errors for each case. Finally, we propose a piecewise polynomial fitting algorithm based on the gradient of the convolution between the foregrounds and the antenna directivity, namely the antenna temperature. This approach was able to keep the residual errors for up to 5 polynomial orders lower than the average expected EoR signal, giving the possibility of positive detection. We applied this algorithm to all the proposed antenna models and filtering strategies and demonstrated using simulated data that the proposed approach can improve the residual level by at least one order of magnitude. This algorithm was applied to simulated data containing the EoR signal and a potential EoR structure was observed.

**Key words:** instrumentation: detectors – dark ages, reionization, first stars

## 1 INTRODUCTION

The low-frequency radio sky from 40–200 MHz has attracted a lot of scientific interest as it can reveal significant information for our cosmic evolution. 21-cm experiments aim to detect the radiation from the redshifted Hydrogen signal originated at the era when the first stars, galaxies, supernovae and black holes were formed and heated the surrounding media. This time is known as the Cosmic Dawn followed by the Epoch of Re-ionization (EoR) when the Inter Galactic Medium (IGM) underwent a violent phase when the neutral (Dark Ages) transitioned to fully ionized Universe. Prob-

ing the 21-cm spin temperature of the hydrogen (rest frequency  $\nu_H = 1420$  MHz) contained in the IGM can provide a window in our cosmic time-line. This cosmic window could potentially reveal the fluctuation of the ionization of the universe by detecting the emission or absorption of the brightness temperature of the redshifted 21-cm line, [Madau et al. \(1997\)](#).

To study the Epoch of Reionization there are two main approaches providing different insights. The first type of experiment is focused on capturing the statistical fluctuations of the 21-cm signal ([Madau et al. \(1997\)](#), [Zaldarriaga et al. \(2004\)](#), [McQuinn et al. \(2006\)](#) [Furlanetto \(2006\)](#), [Morales & Wyithe \(2010\)](#)) and eventually produce an image of the radio sky illustrating areas with high and low ionization. This ex-

\* E-mail:chko@kth.se

periment is based on radio interferometers and there are currently efforts such as the Precision Array to Probe the Epoch of Reionization Array (PAPER, Parsons et al. (2010)), the Murchinson Widefield Array (MWA, Dillon et al. (2014)), the Low Frequency Array (LOFAR, Haarlem et al. (2013) and van Weeren et al. (2016)), the Hydrogen Epoch of Reionization Array (HERA, DeBoer et al. (2017b)) and the Square Kilometre Array (SKA, Carilli et al. (2004) and Dillon et al. (2014)) aiming to detect these fluctuations.

The spatial average of the 21-cm line provides different information (Shaver et al. (1999), Gnedin & Shaver (2004), Sethi (2005), Furlanetto (2006), Pritchard & Loeb (2010b), Morandi & Barkana (2012) and Mirocha et al. (2013)) and as introduced in Bittner & Loeb (2010) an antenna with beamwidth larger than few degrees is capable of capturing the global (average) 21-cm cosmological signal. Efforts such as the Experiment to detect the Global EoR Signal (Edges, Monsalve et al. (2017a)), Broadband Instrument for Global Hydrogen Reionization (BIGHORNS, Sokolowski et al. (2015)), the Shaped Antenna Measurement of Background Radio Spectrum (SARAS, Patra et al. (2013), Patra et al. (2015)), the Large-Aperture Experiment to Detect the Dark Age, Price et al. (2017), are dipole-like based experiments aimed for the global EoR signal. The Dark Ages Radio Explorer (DARE, Burns et al. (2012), Plice et al. (2017)) will be the first satellite based experiment to probe the Dark Ages and Cosmic Dawn orbiting from the lunar farside to avoid terrestrial radio interference.

The model that predicts the the 21-cm signal strength, indicated as brightness temperature  $T_b$ , and relates the mean ionized hydrogen fraction  $\bar{x}_i$  of the IGM, the cosmic microwave background (CMB) temperature  $T_{CMB}$  and the spin temperature  $T_S$  as in (Pritchard & Loeb (2008), Fan et al. (2006), Pritchard & Loeb (2010b)):

$$T_b \approx 27(1 - \bar{x}_i) \left( \frac{T_S - T_{CMB}}{T_S} \right) \sqrt{\frac{1+z}{10}} \text{ mK.} \quad (1)$$

The redshift  $z$  depends on the fraction of the ionized hydrogen gas and the  $T_S$ . For the 21-cm line the redshifts correspond to  $6 \leq z \leq 27$  translated to the frequency interval  $\nu = 200 - 50$  MHz referenced to the resting frequency of the hydrogen.

Based on the model for the expected signal for the global 21-cm signal, the sensitivity of the instrument should be  $\geq \sim 1$  mK for successful and reliable detection, that is coherent with the theoretical predicted levels of the signal and it is further motivated in the work of Monsalve et al. (2017a). In addition to the required sensitivity, the signal is contaminated by the diffuse galactic radio emission or foregrounds that is orders of magnitude larger than the expected EoR signal. The foregrounds are expected to be spectrally smooth following a simple power law, de Oliveira-Costa et al. (2008). This spectral smoothness gives the possibility that the foregrounds could potentially be subtracted from the received signal. However, when the radiation pattern of the antenna is also taken into account, this results in a spectrally varying function that severely impacts the foreground calibration. In addition, the presence of foregrounds imposes a design consideration on the antenna and is required to be included for the calibration of the experiment (see Bernardi et al. (2015), Mozdzen et al. (2016)).

In this work we focus on both the impact of the antenna

and the foreground removal for the calibration of the system. The response of the antenna varies across its frequency of operation resulting in different radiation patterns. This is typically referred to as "antenna chromaticity". Since the antenna represents the first block of the experimental set up at any radiometer, any non-linear behaviour will propagate through the entire radiometer. This shows the importance of modeling and proper calibration of the antenna system at any radiometer. The basic definitions of the quantities utilized throughout this work are given in section 2. In Section 3, we study the impact on the antenna temperature and the possibility of global EoR detection using realistic antenna models. We divide the antenna models into two different classes based on their angular resolution capabilities and we use the analytical description of the ideal dipole over an infinite ground plane as a reference case. In addition, in Section 4, we explore the effect of the foreground modeling and its impact on the 21-cm line detection. Three popular foreground models found in the literature are evaluated utilizing the proposed antennas. In Section 5 we propose a piecewise polynomial fitting algorithm based on the gradient of the antenna temperature. This approach can serve as an exit strategy to account for the chromatic behavior of the antenna. Modeling of additive noise as measurement uncertainty and filtering strategies are also explored. The basic measurement of the global EoR signal remains to be verified and initial results are presented in the recent work of Bowman et al. (2018). In the subsequent work by Hills et al. (2018) further discussion is provided on the strong influence of the foreground modeling on those results and the effect of polynomial fitting. This work can provide a simple post processing algorithm for an experimental set up to calibrate the overall antenna receiver response.

## 2 ANTENNA TEMPERATURE IN THE PRESENCE OF FOREGROUNDS

The global EoR experiment is based on measuring the received power of an antenna receiver system. This received power is typically referred to as antenna temperature and is captured by the antenna pointed at the sky and measured with a calibrated receiver. In a given time  $t$  the overall system temperature is given for a direction  $\hat{n}$  as in Warnick et al. (2010):

$$T_{sys}(t, \nu, \hat{n}) = T_{rec}(t, \nu) + \eta(t, \nu)T_{ant} + (1 - \eta(t, \nu))T_0, \quad (2)$$

where  $\nu$  is the frequency,  $T_{rec}$  is the receiver's temperature,  $T_{ant}$  the antenna temperature multiplied with an efficiency  $\eta(t, \nu)$  that combines the receiver gain and the antenna efficiency. We denote as  $T_0$  the physical antenna temperature. Note that we disregard any temporal efficiency dependency factors such as metal oxidization, dust etc, since they are slow varying and can be accounted by recalibrating the system at regular time periods. We follow a similar system decomposition for the system temperature as in Warnick et al. (2010). This definition isolates the impact of the foregrounds and the antenna pattern response providing a useful measure to study the antenna temperature separately. The antenna temperature  $T_{ant}$  is defined as:

$$T_{ant}(\nu, \hat{n}) = \frac{1}{4\pi} \int_{\Omega} D(\mathbf{s}, \hat{n}) T_{sky}(\mathbf{s}) d\Omega \quad (3)$$

and is a convolution between the radio sky temperature  $T_{sky}$  and the antenna directivity pattern  $D(\mathbf{s}, \hat{n})$ . In this work, we assume a time invariant beam pattern and an infinite perfect electric conductor (PEC) as ground. Any ground imperfections as well as the ground finiteness are not part of this work. Additional environmental effects, such as rain are also not considered since in such events the data obtained are disregarded. The radio sky, at the frequencies of interest where the EoR is expected, is dominated by synchrotron emission, [Matteo et al. \(2002\)](#), [McQuinn et al. \(2006\)](#). The foregrounds have a smooth frequency dependence, which is further discussed in Section 4, that follows a power law. A logarithmic polynomial fit of the foregrounds, similar to the 21cm tomography proposed in the works of, [Pritchard & Loeb \(2010a\)](#), [Wang & Hu \(2006\)](#) such as:

$$\log \hat{T}_{fg}(\nu) = \sum_{n=0}^m \alpha_n (\log \nu)^n, \quad (4)$$

where the  $\hat{\cdot}$  denotes the estimated data is used in this analysis as the foreground removal scheme. In turn we evaluate the residuals of the polynomial fit and the antenna model according to the figure of merit FoM:

$$FoM(t, \nu, \hat{n}) = \sqrt{|T_{ant}(t, \nu, \hat{n}) - \hat{T}_{model}(t, \nu, \hat{n})|^2}. \quad (5)$$

Realistically to balance uncorrelated sky and receiver noise we take the average spectrum over a period of time  $\Delta t$  as:

$$T(\nu, \hat{n}) = \frac{1}{\Delta t} \int_t^{t+\Delta t} T(t, \nu, \hat{n}) dt \quad (6)$$

and we evaluate the time averaged residuals according to:

$$\langle FoM(\nu, \hat{n}) \rangle = \sqrt{|\langle T_{ant}(\nu, \hat{n}) \rangle - \hat{T}_{model}(\nu, \hat{n})|^2} \quad (7)$$

and the total RMS residual from

$$\langle FoM(\hat{n}) \rangle = \sqrt{|\langle T_{ant}(\hat{n}) \rangle - \hat{T}_{model}(\hat{n})|^2}, \quad (8)$$

where  $\langle \dots \rangle$  denote the average. For successful detection the residuals from the equations 7 and 8 should be below the expected level of the EoR signal  $< \sim 10$  mK. Low order polynomials are required in order to subtract only the largest Fourier modes of the foreground signal. We also define the differential residual as in equation (9) that represents the difference between the antenna temperature response and the predicted response. Ideally the differential residuals should follow a random distribution for accurate data fitting.

$$Diff\ Res(\nu, \hat{n}) = \langle T_{ant}(\nu, \hat{n}) \rangle - \hat{T}_{model}(\nu, \hat{n}). \quad (9)$$

In this work we evaluate the impact on the residuals of the current up-to-date radio sky models along with the antenna beam chromaticity for different antenna models. Our aim is to provide a rigorous methodology for detecting the EoR signal with realistic antenna and sky models.

### 3 ANTENNAS

To study the effect of the antenna chromaticity on detection of the global EoR signal we evaluate five different antennas. In particular, we evaluate the theoretical model of a horizontal dipole over an infinite ground plane, [Balanis](#)

**Table 1.** Summary of the properties of the evaluated antennas. The indicated properties are the min and max directivity  $D$  on a dB scale, the voltage standing wave ratio VSWR, and the angular resolution.

Antenna	Antenna Property			
	min $D$	max $D$	VSWR	Ang. res.
Ideal dip.	3	7	-	Low
Bow-tie dip.	3	8	2.5	Low
SKALA	3	9	2.6	Low
HERA	6.5	29	2.2	High
CLDA	7	30	2.2	High

(2005), a simulated realistic bow-tie like dipole, [Yang et al. \(2016\)](#), the SKALA antenna that is a log periodic antenna, [de Lera Acedo et al. \(2015\)](#), the HERA antenna which is a reflector antenna, [DeBoer et al. \(2017b\)](#), and a capacitively loaded antenna array - CLDA which is a simplified design based on our previous work, [Kolitsidas et al. \(2014\)](#). The selected antennas are representative candidates for the EoR signal with two, namely the HERA and SKALA to be directly involved in instruments that are being deployed to detect the fluctuations of the EoR signal. In this work the model used for SKALA is SKALA1 and currently the SKALA4 is underdevelopment. Bow-tie like dipole have also been used in the Murchison Widefield Array - MWA as the SKA precursor, [Neben et al. \(2016\)](#). We further classify the selected antennas into two categories based on their respective capabilities of angular resolution. We focus only on the chromatic beam effects of each antenna. The fundamental descriptive properties of the antennas are summarized in Table 1. The receiver chain can further be calibrated similar to Edges, [Monsalve et al. \(2017a\)](#).

In the work of [Liu et al. \(2013\)](#) it was shown that a high angular resolution antenna could have a higher likelihood to detect the global EoR, however this prospect has not yet been fully exploited and the current experiments are based on a dipole like antennas. In the same work, real chromatic effects of high angular resolution antennas were also not considered. This further motivates our antenna classification based on their angular resolution and study their respective effects on antenna temperature.

The realistic antennas have been simulated with the time domain finite integral method solver from CST - MWS (Computer Simulation Technology - Microwave Studio, [CST \(2016\)](#)), with the exception of the ideal dipole that is analytically described. Standard sensitivity testing was performed to verify that during the simulations no solver numerical resonances occur and we obtain smooth convergence. The antennas are assumed to be located in the South African Karoo Astronomy Reserve, with coordinates approximately  $30.71^\circ S$  and  $21.45^\circ E$ . In all simulations we have used an infinite perfect electric conductor as ground plane to isolate the beam chromaticity from the antenna shape and evaluate the corresponding antenna class.

#### 3.1 Low Angular Resolution Antennas

Global 21-cm experiments have, so far, been utilizing primarily wide beam antennas such as dipoles. This results in sampling the radio sky with low angular resolution. We de-

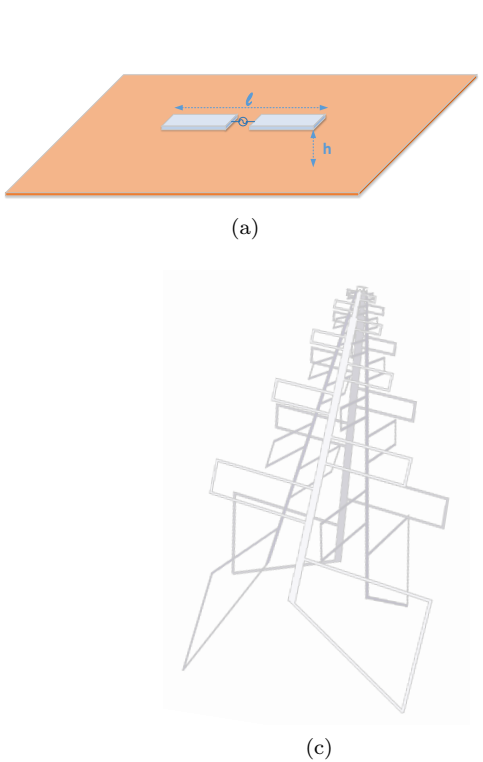


**Figure 1.** Antenna schematics for (a) ideal dipole (b) simulated dipole (c) SKALA.

fine low angular resolution antennas in this study as antennas that have half power beamwidth - HPBW > 20° and we include in the following analysis the ideal dipole, the simulated dipole and the SKALA.

The directivity of the simple horizontal dipole over an infinite ground plane can be described by the analytical formula based on Balanis (2005):

$$D(\theta, \phi) = 4 \sin^2(kh \cos \theta)(1 - \sin^2 \theta \sin^2 \phi)/R, \quad (10)$$

$$R = \left[ \frac{2}{3} - \frac{\sin(2kh)}{2kh} - \frac{\cos(2kh)}{(2kh)^2} + \frac{\sin(2kh)}{(2kh)^3} \right], \quad (11)$$

where  $\theta, \phi$  are the elevation and azimuthal angles,  $\lambda$  is the wavelength,  $h$  is the distance over the ground plane and  $k = 2\pi/\lambda$  is the wavenumber. A schematic representation of the dipole is depicted in Fig. 1a. The beam chromaticity is a slowly varying function based at the frequency dependent ratio  $kh$ . It is worth noting, that we do not approximate the equation (11) since it will not hold for the entire frequency band that the dipole is evaluated over. The parameter  $h$  is selected within the range  $\lambda_{h\nu}/3 < h < \lambda_{h\nu}/2$ , where  $h\nu$  we denote the high end of the frequency band. This constraint ensures that only one lobe is achieved within this frequency range minimizing the antenna chromaticity. The obtained beam pattern is illustrated in Fig. 2a at 150 MHz projected into the celestial sphere in equatorial coordinates. We motivate the inclusion of this model in the present study as a reference case for slowly varying chromatic beams compared to a realistic antenna model.

The second model is a realistic bow-tie like dipole antenna. Bow-tie dipoles utilize tapering to improve the band-

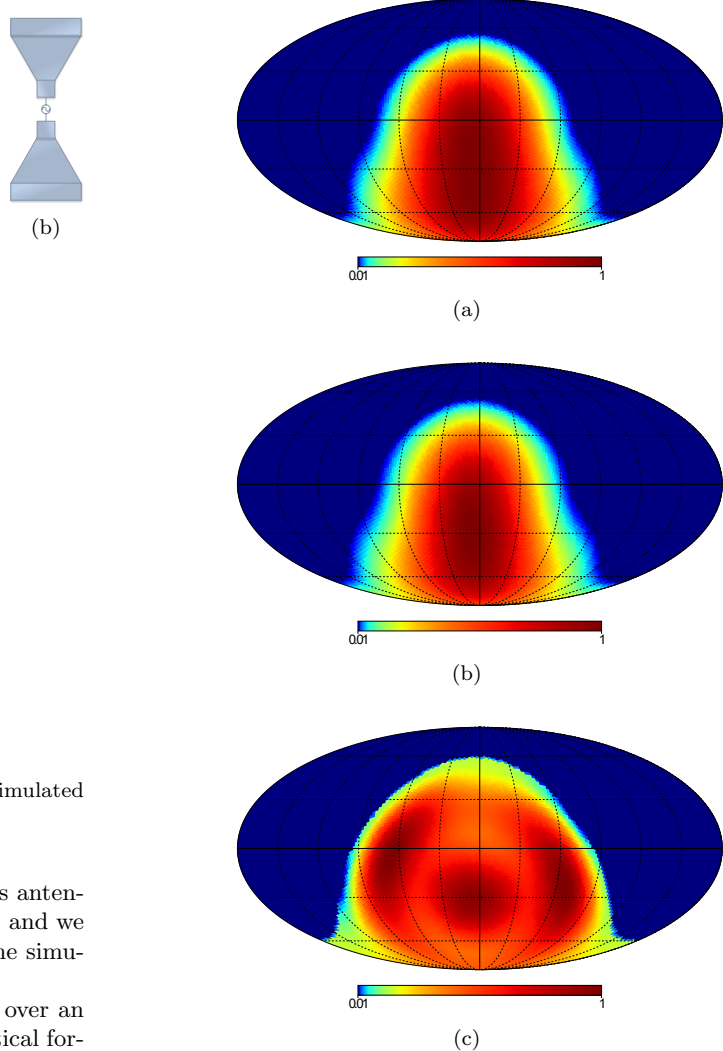


**Figure 2.** Normalized antenna directivity pattern at 150 MHz projected into the celestial sphere in equatorial coordinates for the (a) ideal dipole over a ground plane from (b) dipole simulated in CST (c) SKALA.

width performance over the standard dipole. This antenna will be benchmarked directly with the ideal dipole to observe the differences in the performance as global EoR probes. In order to have a fair comparison we used the same dimensions with the ideal dipole and only optimized the width and the tapering. As previously discussed, differences in the distance over the ground plane will result in different chromaticity in the upper half of the frequency band. The schematic of the designed dipole antenna is depicted in Fig. 1b. The resulted beam at 150 MHz as projected into the celestial sphere in equatorial coordinates is depicted in Fig. 2b.

The final antenna evaluated in the subclass of the low angular resolution antennas is a single SKALA antenna. This is a variation of a dual-polarized log periodic dipole antenna array. This type of antennas is able to provide the appropriate bandwidth to probe the EoR with very good inherent impedance matching. An illustration of the SKALA is depicted in Fig. 1c. The benefit of the SKALA antenna is that part of the reflector is integrated in the antenna for the most part of the frequency band minimizing the soil

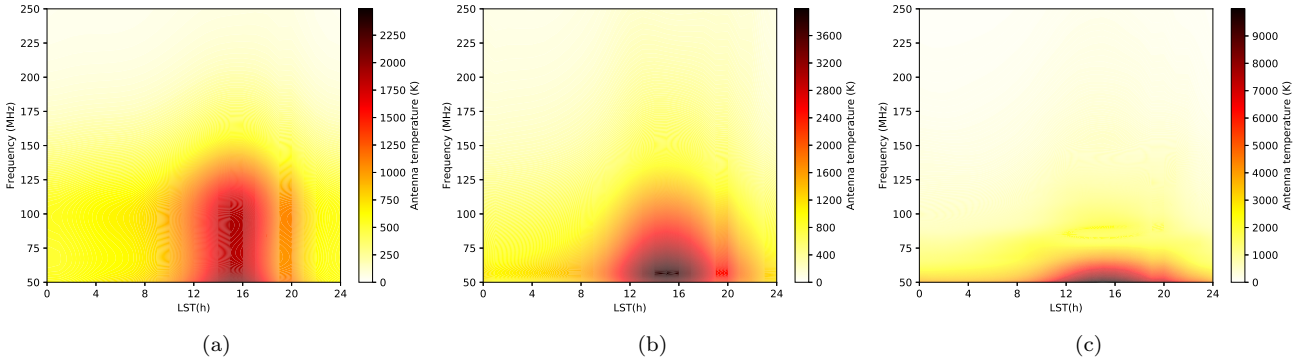


**Figure 3.** Waterfall diagram for the simulated antenna temperatures for a single day (22/07/2018) located in the Karoo of (a) ideal dipole (b) simulated dipole (c) SKALA. Note the difference the scales for the antenna temperature.

and ground effects. The SKALA antenna has not been designed to be used as a stand alone antenna but as part of phased array and furthermore it has been designed to cover a large frequency band (7:1), and to provide high sensitivity, which inherently introduces some level of chromaticity on the antenna performance. An analysis of the chromaticity requirements for SKA and the SKALA design can be found in [de Lera Acedo et al. \(2017\)](#). This effect is clearly visible with the sidelobes appearing in the radiation pattern as depicted in Fig. 2c. The SKALA choice can be considered as a more advanced but realistic implementation of the ideal dipole as we can achieve better impedance matching.

To evaluate the time interval when measurement can be obtained we evaluate the waterfall diagram of the antenna temperature for 24 h. The waterfall diagrams for the low angular resolution antennas are illustrated in Fig. 3 where we note the different scales for each antenna. There is approximately an 800 K difference between the ideal dipole model and the simulated bow-tie dipole as depicted in Fig. 3a and Fig. 3b. The antenna temperature of the SKALA, see Fig. 3c is approximately 2000 K higher due to the enhanced directivity. The differences at the scales of the antenna temperature are attributed to the difference in the corresponding directivity of each antenna. Based on the waterfall diagrams we simulate virtual antenna temperatures between 0:00-4:00 LST for every 15 min for an 8 day span. In this time window we observe lower antenna temperature as the galactic center is at or below the horizon. These data are then used for all calculations referred in this work and are based on equation (7). The 8 day span is selected to simulate the conditions of a realistic experiment and further smoothen the antenna temperature. This was also indicated in the work of [Bowman et al. \(2018\)](#).

### 3.2 High Angular Resolution Antennas

An alternative to wide beam antennas described in the previous section 3.1 are the high gain antennas with very narrow beamwidth. These antennas can offer very high angular resolution and have not yet been explored extensively in the literature. Antennas that naturally fall into this category are reflector antennas, lens antennas and antenna arrays. Lens antennas are typically based on dielectrics and this

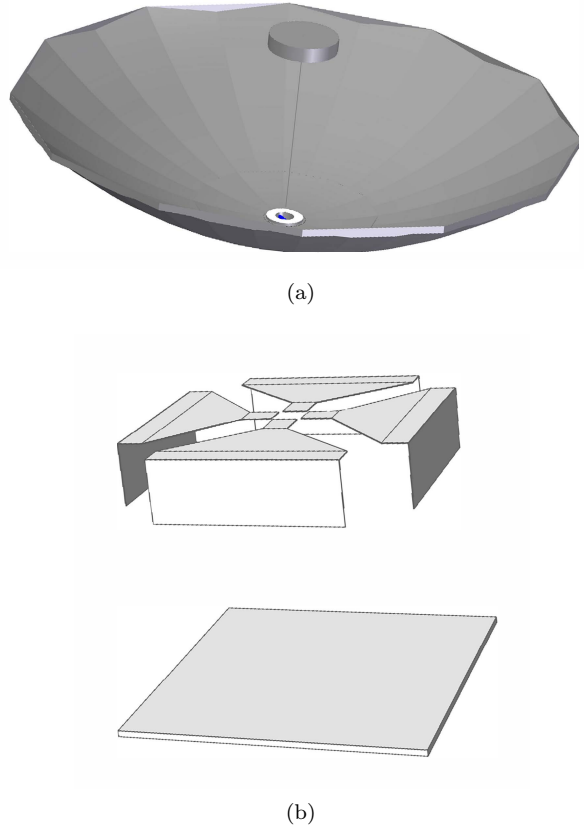


**Figure 4.** Illustration of the antenna design of (a) HERA (b) the unit cell of the CLDA.

will add to the thermal noise of the antenna hence will not be explored further here. The main benefit of a well designed highly directive antenna is that the field of view can be aligned with cold patches of the sky.

As a first model to evaluate from the class of high angular resolution antennas comes from the reflector type antennas and specifically we evaluate a single HERA reflector antenna, [DeBoer et al. \(2017a\)](#). Reflector antennas have a long and successful history in radio astronomy. The HERA antenna is a reflector with no mechanically moving parts and the beam oriented always to the antenna zenith. The feeder

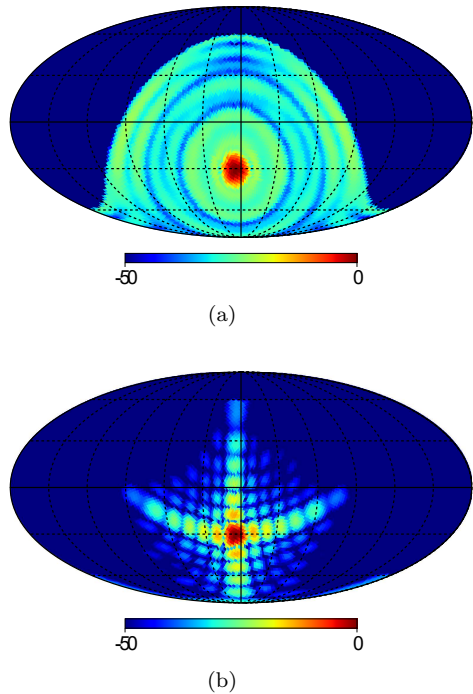


**Figure 5.** Normalized antenna directivity pattern in dB scale at 150 MHz for (a) simulated HERA (b) simulated CLDA with uniform aperture illumination.

for the HERA are the "recycled" Precision Array for Probing the Epoch of Reionization (PAPER, Parsons et al. (2010)) dipoles. The design is depicted in Fig. 4a. This design has the benefit that the majority of the collected sky signal is reflected from a metallic mesh to the focal point. Therefore the effects of the surroundings and the ground are minimized. In addition, the HERA's high gain narrow beamwidth with low sidelobes will provide better receiver sensitivity. The simulated normalized beam as projected into the celestial sphere for 150 MHz is illustrated in Fig. 5a.

Finally we evaluate a dense fully populated capacitively loaded dipole array as an alternative solution of the aforementioned. In Fig. 4b the designed array's unit cell is illustrated. The array is dual polarized and consists of  $25 \times 25$  elements per polarization totaling an overall 1250 element ports. The corresponding normalized beam as projected into the celestial sphere for 150 MHz is illustrated in Fig. 5b where the  $\sin x/x$  pattern of uniform aperture illumination is clearly visible. The proposed CLDA can provide similar bandwidth to the SKALA and HERA but in addition has the possibility to be fully flexible, i.e. the beam can scan only cold patches of the sky. This reduces the integration time and improves the required stability from the receiver electronics. This also implies that there are fewer possibilities of different conditions in the electronics and in the surrounding environment. One more benefit of the CLDA is that one can obtain reduced chromaticity of the array beam by employing wavelength scaling sub-arrays to have an almost constant beamwidth across the frequency band. The CLDA was designed to have almost the same physical area as the HERA. The obvious disadvantage of the CLDA is the required control points, hence it is an expensive solution.

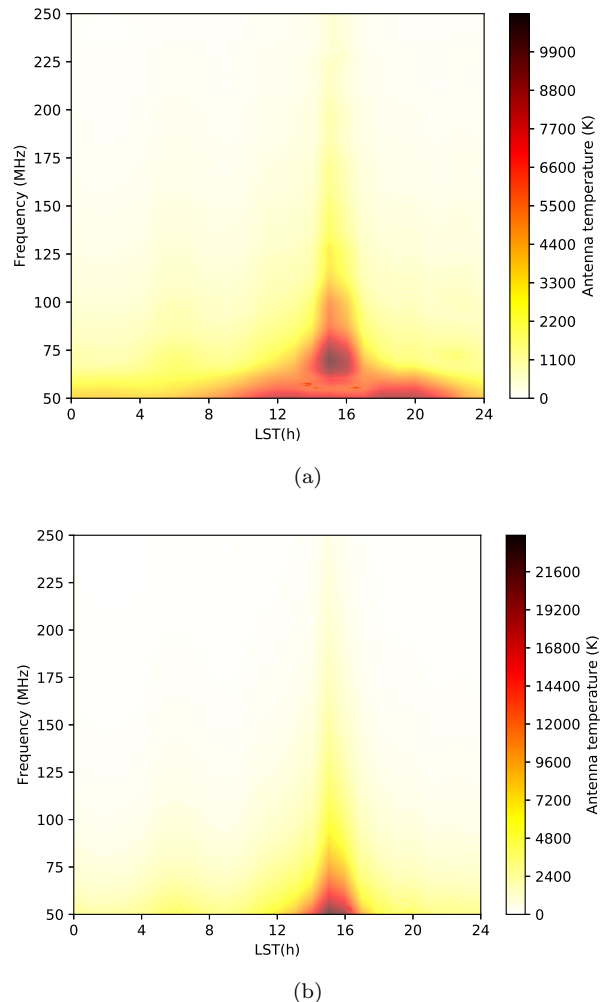


**Figure 6.** Waterfall diagram for the simulated antenna temperatures of (a) HERA (b) CLDA.

Another possibility that can be considered is a mechanically steerable reflector or a reflector with a phased array feed.

The last step is to evaluate the corresponding antenna temperature over the course of a full day to find the time interval of observation. This is similar to the low angular resolution antennas of Section 3.1 and will provide us an observational time frame. In Fig. 6 the waterfall diagrams for the antenna temperature are depicted. We observe that when the galactic centre is at the antenna zenith the CLDA has double the antenna temperature compared to the HERA antenna. On the contrary, during the observation time (0:00–4:00 LST) the CLDA and the HERA antenna temperature is similar and approximately 1500 K. It is also observed that in the low frequencies ( $\nu \in [50 - 75] \text{ MHz}$ ) the HERA antenna has higher antenna temperatures than the CLDA.

#### 4 SKY MODELS

At the frequencies where the global EoR is expected (100–200 MHz) the radio sky is dominated by synchrotron emission Jelić et al. (2010). The properties of the foregrounds at these frequencies have only been physically modeled so far, and detailed measured sky maps are yet remained to

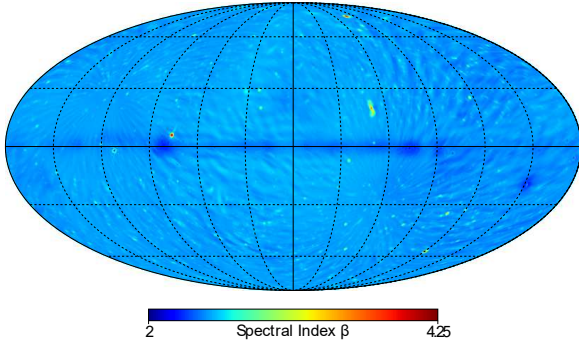


**Figure 7.** Spectral Index  $\beta$  in galactic coordinates.

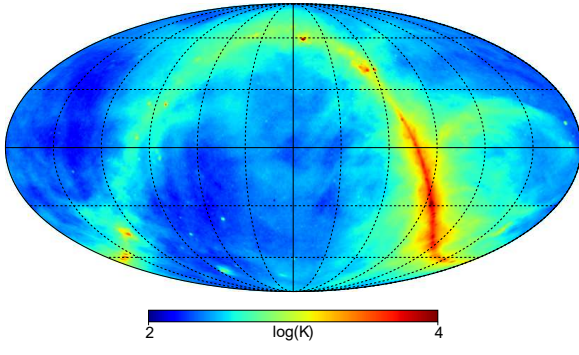


**Figure 8.** 150 MHz scaled Haslam map in equatorial coordinates using the angular dependent spectral index  $\beta$  from Fig. 7.

be established. The synchrotron emission has been proven to follow a simple power law relation, Jelić et al. (2010), and the scaling factor is usually referred to as the spectral index  $\beta$ . Equation (12) reads the frequency scaling relation of the radio sky referenced to the entire sky survey of the 408 MHz Haslam map Haslam (1982). The cosmic microwave background - CMB is not scaled and we have used the Planck data, Adam et al. (2015), for the CMB performing the operation at every pixel. The scaled map for each frequency  $\nu$  is given as:

$$T_{sky}(\nu, \mathbf{s}) = (T_{Sky\ Model}(\mathbf{s}) - T_{CMB}) \left( \frac{\nu}{\nu_{sky}} \right)^{-\beta} + T_{CMB}. \quad (12)$$

To evaluate the impact of the sky models on the detection of the EoR signal, we have used two different models representing two extreme cases. The first sky model is the unfiltered - NF version of the Haslam map, Haslam (1982). A constant spectral index  $\beta = 2.5$  is used in this approach, as has been extensively used in the literature Matteo et al. (2004), Rogers & Bowman (2008) and Bowman et al. (2009). This model represents a noisy sky model and will provide a lower bound on the residuals in this study. The second sky model is the widely used destriped desourced - DSDS updated Haslam map from Remazeilles et al. (2015). To account for the angular dependency we adopt the technique similar to Bernardi et al. (2015) and Mozdzen et al. (2017),

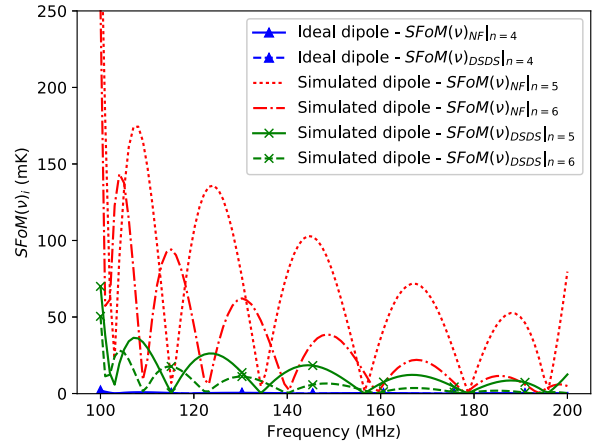


**Figure 9.** Residuals for the theoretical dipole model and the simulated bow-tie dipole model.

where the spectral index is extracted according to equation:

$$\beta = - \left[ \ln \left( \frac{T_{sky\ \nu_\beta} - T_{CMB}}{T_{sky\ 408MHz} - T_{CMB}} \right) / \ln \left( \frac{\nu_\beta}{408} \right) \right], \quad (13)$$

where  $T_{sky\ \nu_\beta}$  refers to the the sky as extracted from de Oliveira-Costa et al. (2008) whereas the  $T_{sky\ 408MHz}$  is the DSDS Haslam map. This approach provides a better estimate of the spectral index for every pixel. In contrast to the work of Mozdzen et al. (2017) where measured data were used to correct the values of the spectral index for the LST, whereas in Bernardi et al. (2015) the CMB was not taken into account. The result of this ratio (Eq. (13)) is depicted in Fig. 7 in galactic coordinates, where we observe that the spectral index is not uniform across the entire sky when calculated pixel by pixel. In this work, the spectral index is calculated only for a single frequency at  $\nu_\beta = 100$  MHz. The scaled Haslam map at 150 MHz with varying spectral index is illustrated in Fig. 8 in equatorial coordinates. A straightforward extension to this method is to obtain the spectral index for each frequency following the same procedure using equation (13). This will also account for the frequency variants of the spectral index. From the illustration of the spectral index in Fig. 7, it is expected that the varying spectral index is more suitable for the high angular resolution antennas as only a small part of the sky is sampled with the antenna beam whereas a constant spectral index can be utilized in the low angular resolution antennas as the effect will be averaged out. To illustrate this effect we define the sky figure of merit  $SFoM(\nu)_i$  as in equation:

$$SFoM(\nu)_i = \sqrt{\left| T_{ant}(\nu)_i - \hat{T}_{ant}(\nu) \right|^2}, \quad i \in \{NF, DSDS\}, \quad (14)$$

where we test the root mean square (rms) error for each antenna model of the estimated value and the polynomial fit in the entire band for each sky model. In the following analysis the two sets  $\{NF\ \text{map}, \beta = 2.5\}$  and  $\{DSDS\ \text{map}, \beta = \text{Fig. 7}\}$  are used and the corresponding set is indicated by the map choice as a subscript.

The ideal dipole and the simulated bow-tie dipole are evaluated and the results are presented in Fig. 9. We observe

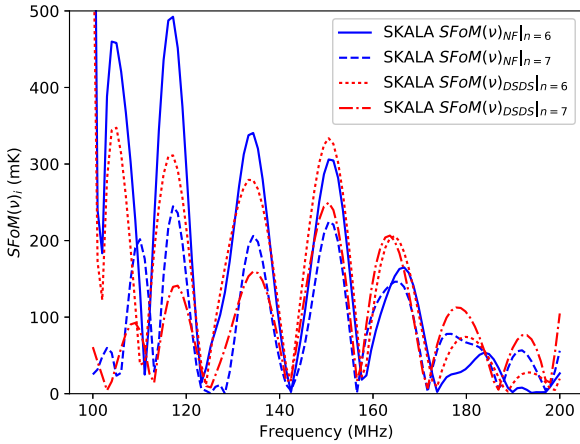


**Figure 10.** Residual for the SKALA model for the different sky models.

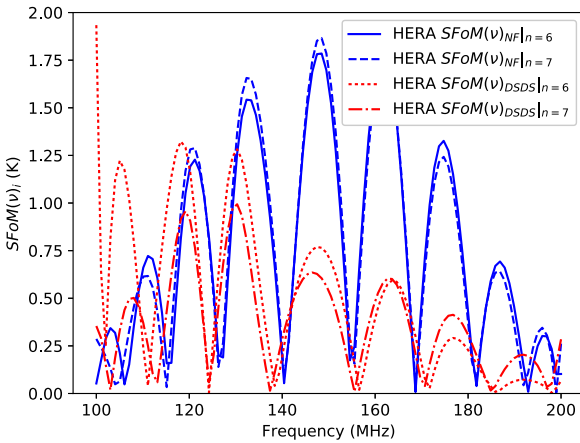


**Figure 11.** Residual for the HERA model for the different sky models.

that for the ideal dipole the rms error is very small ( $\leq 5$ ) mK in both sky models evaluated as well as for only  $4^{th}$  order polynomial fit. The results are illustrated in the zoomed area in Fig. 9. The reason for this behavior is traced to the slowly varying function that represents the ideal dipole. In contrast, the simulated bow-tie like dipole has a more severe impact on the rms error between the fitted data and the calculated. We observe that the average  $\langle SFoM(\nu)_{DSDS} \rangle = 17$  mK whereas is about  $\langle SFoM(\nu)_{NF} \rangle = 36$  mK for  $6^{th}$  order polynomial fitting. This is an indication of the impact of sky model on the calibration of the instrument. In addition, even though the ideal dipole has very low residuals it is hardly the case for a representative realistic antenna model. This implies that in the design of the global EoR experiment the chromatic antenna behavior should be taken into account.

The impact of the antenna chromaticity in the SKALA case is illustrated in Fig. 10, with the data are fitted over the entire frequency interval. The averaged  $\langle SFoM(\nu)_{NF} \rangle = 104$  mK and  $\langle SFoM(\nu)_{DSDS} \rangle = 82$  mK for a  $7^{th}$  order polynomial fitting. These differences stem from the antenna beam chromaticity of the SKALA as well as the limited simulated time interval of observation.

The residual for the case of the HERA reflector antenna

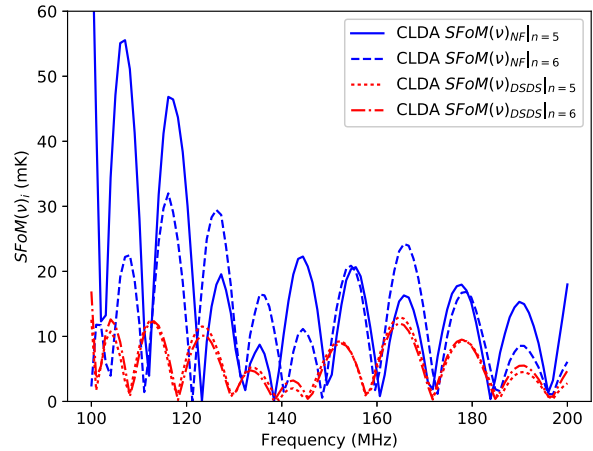


**Figure 12.** Residual for the CLDA model for the different sky models.

are presented in Fig. 11. Here note that the scale on the  $SFoM(\nu)_i$  axis is K. We observe that the  $\langle SFoM(\nu)_i \rangle$  becomes  $\langle SFoM(\nu)_{NF} \rangle = 1.14$  K and  $\langle SFoM(\nu)_{DSDS} \rangle = 0.5$  K for a  $7^{th}$  order polynomial fitting. We have traced two reasons for this behavior. The first reason is that the impact of the angular dependency of the sky model becomes more pronounced for a high angular resolution antenna and the second reason is that the HERA radiation pattern does not follow any known smooth function. The impact of a noisy, with no angular resolution sky model is visible in Fig. 12 for the case of CLDA. In this case we have used the uniform aperture illumination that results in beams that follow the smooth bandlimited function of  $\text{sinc}(x)$ . The average sky  $FoM$  becomes  $\langle SFoM(\nu)_{DSDS} \rangle = 8$  mK for a  $6^{th}$  order polynomial fitting that is the lowest for all realistic evaluated antenna models in this study.

Following the earlier discussion, we can conclude that when a high angular resolution antenna is utilized it is important to use a sky model that provides angular resolution as well, as proposed in this study. In addition, the smoothness of the antenna beam severely impacts the overall rms fitting error and special care needs to be taken during the design of the antenna. In continuance we propose an exit strategy to overcome the antenna beam smoothness limitation.

## 5 PIECEWISE POLYNOMIAL FITTING BASED ON THE ANTENNA CHROMATICITY

In the previous section, the impact of the sky model on the antenna temperature was evaluated. Through this study it was also shown that fitting the antenna temperature over the entire bandwidth on a realistic model gives rise to very high residuals and the power spectrum of the antenna and the foregrounds severely contaminate the global EoR signal. To overcome this limitation and keep integration times short we propose a piecewise fitting scheme that follows the behavior of the antenna temperature. In Monsalve et al. (2017b) there is a discussion that the bandwidth reduction will result in lower residuals however the motivation was to focus on the

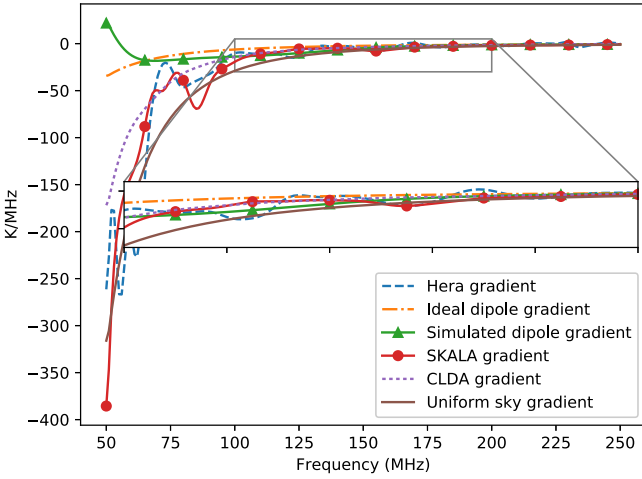


**Figure 13.** Antenna temperature gradients for all antenna models and the sky gradient, note the magnified area of the global EoR interval.

**Table 2.** Calculated  $CFoM$  for each antenna model for the global EoR frequency interval.

	Dipole	SKALA	HERA	CLDA
$CFoM$	2	6	9	2

peaks of the EOR signal. Since the antenna chromaticity will impact the antenna temperature in a non systematic way, this will influence the magnitude of the residuals across the frequency interval. The impact on the antenna of the beam chromaticity, denoted here as  $T'_\nu$  can be analyzed by taking the gradient of the time averaged antenna temperature  $\langle T_{ant} \rangle_t$ .

$$T'_\nu = \nabla \langle T_{ant} \rangle_t, \quad (15)$$

where from the above equation we can further define the antenna chromatic figure of merit  $CFoM$  as the number of inflection points - IP in the overall bandwidth of observation of the  $T'_\nu$ .

$$CFoM = \text{No. of } \{\text{inflection points } T'_\nu\} \left| \frac{\partial^2 \langle T_{ant} \rangle_t}{\partial \nu^2} \right| = 0. \quad (16)$$

For an antenna of no chromatic effect in the bandwidth of operation this is equal to zero as the antenna temperature follows the power law of the spectral index. We approximate the  $\langle T_{ant} \rangle_t$  with a piecewise logarithmic polynomial fit based on the  $CFoM$  in the total bandwidth  $[\nu_{low}, \nu_{high}]$  such as:

$$\log T_{fg} = \begin{cases} \sum_{n=0}^m \alpha_n (\log \nu_1)^n & \text{for } \nu_1 \in [\nu_{low}, \nu_{1^{st} IP}] \\ \cdot \\ \cdot \\ \sum_{n=0}^m \alpha_n (\log \nu_i)^n & \text{for } \nu_i \in [\nu_{i^{th} IP}, \nu_{high}]. \end{cases} \quad (17)$$

To illustrate the impact of the beam chromaticity the gradient of the antenna temperature is shown in Fig. 13

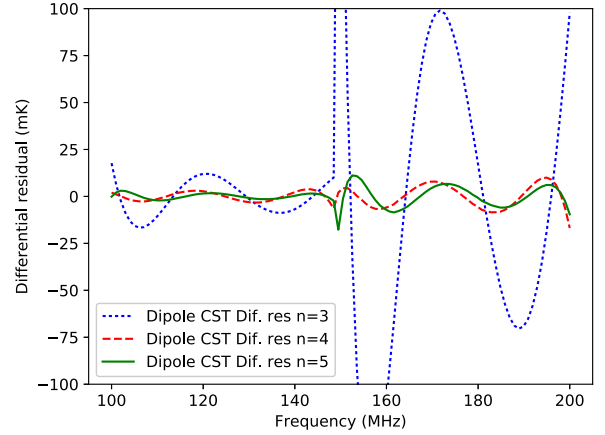


**Figure 14.** Differential Residuals for the simulated CST dipole model.

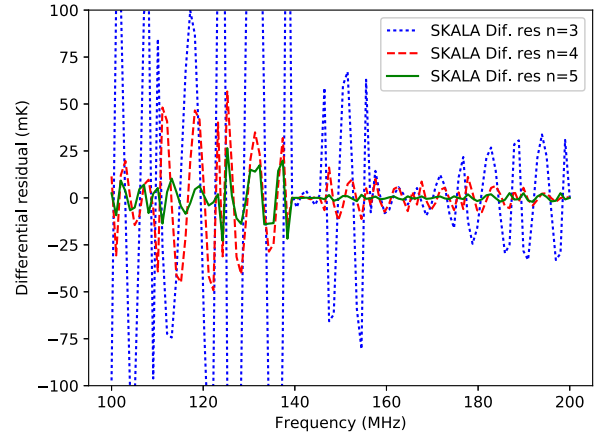


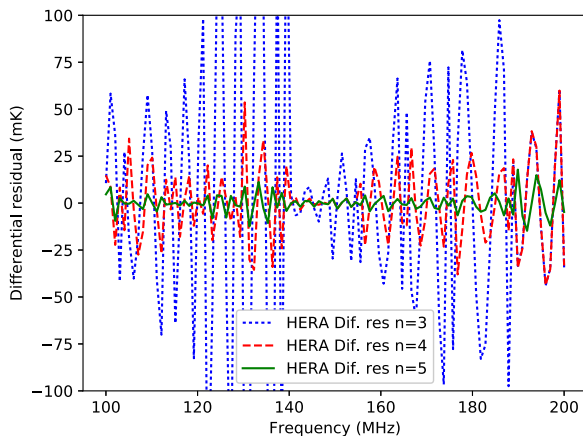
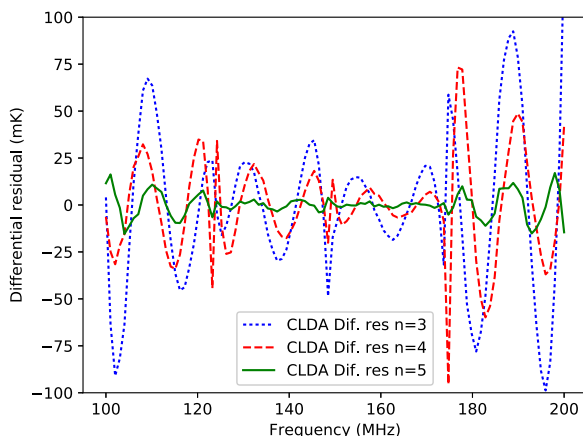
**Figure 15.** Differential Residuals for the SKALA model.

where the sky gradient is also shown. Rippling is observed for the SKALA and HERA antennas. This was expected from the results of Section 4 and here we show a tool that can easily illustrate the expected behavior of any antenna model. The simulated dipole and the CLDA appear smoother as anticipated. The results of the  $CFoM$  according to equation (16) are tabulated in Table 2. Ideally the  $CFoM$  should be zero to follow the foreground's power law otherwise it represents concavity alteration (polynomial order  $\geq 3$ ). The  $CFoM$  can be utilized as an indicator of the antenna performance as a probe for the global EoR. The  $CFoM$  can be extended as an indicator of the overall antenna performance for the entire experiment and evaluate the system temperature from equation (2). In this case the overall gradient of the experiment is hardly expected to follow the foreground power law, even if the antenna directivity does, since factors such as the efficiency and the receiver gain will have non linear effects on the antenna temperature. The proposed piecewise polynomial fitting algorithm presented in this section can be an exit strategy for all global experiments and can be applied in the end of the receiver chain.

In order to provide further insight of the proposed algorithm, it is applied to the data of Section 4 according to equation (17) and the  $CFoM$ . In Fig. 14 the differential

**Table 3.**  $\langle F_{\text{oM}}(\hat{n}) \rangle$  in mK for the 5<sup>th</sup> polynomial order for antenna models with simulated pattern noise and filtering.

	Dipole	SKALA	HERA	CLDA
Ideal pattern	3.152	4.403	3.664	4.408
0.5dB beam noise	3.427	5.061	4.842	5.281
0.1dB beam noise	3.215	4.587	3.978	4.623
0.5dB noise S.G. filter	3.346	4.483	3.814	4.511
0.1dB noise S.G. filter	3.192	4.434	3.681	4.454
0.5dB noise C-H filter	3.352	4.762	3.701	4.466
0.1dB noise C-H filter	3.211	4.589	3.673	4.421

**Figure 16.** Differential Residuals for the HERA model.**Figure 17.** Differential Residuals for the CLDA model.

residuals of the dipole are illustrated, where it is observed that for a 5<sup>th</sup> order polynomial the residual become very small ( $\leq 3$  mK) for the lower half of the band and ( $\leq 7$  mK) for the upper half. At 148 MHz a monotonicity alteration is observed and the spike that is apparent in Fig. 14 is observed. Similarly, the differential residuals for the SKALA are presented in Fig. 15 where only the part between 120–140 MHz appears to have residuals ( $\leq 20$  mK) that will result in successful detection of the global EoR for the simulated data in this work. Finally, in Fig. 16 and in Fig. 17 the differential residuals are represented for the HERA and the CLDA

model. It is observed that low residuals appear in both cases ( $\leq 15$  mK) with the HERA to be able to have the advantage for the global EoR detection for the entire frequency interval keeping residuals ( $\leq 3$  mK) for a 5<sup>th</sup> order polynomial. In this calculation the HERA residuals are lower than the CLDA as the frequency interval is spliced 12 times instead of two in the CLDA.

All the above calculation are performed with eight days of data of four hours observation time per day according to equation (6) to further reduce the impact of the foreground differences and average out its impact. The presented results can further be reduced by adding more observation time.

### 5.1 Impact on the Antenna Radiation Pattern Measurement Errors and Filtering Strategies

To accurately calibrate the instrument, detailed measurements for the antenna radiation pattern are required. Typical antenna measurements take place in a controlled environment such as an anechoic chamber. However in the case of the global EoR cosmological experiment due to the physical antenna size measurements are typically performed with the help of a drone that carries a probe, De Lera Acedo et al. (2018) and Pupillo et al. (2015). Interferometric measurements have also been used in LEDA, Price et al. (2017). It has been shown in Pivnenko et al. (2009) and Saporetti et al. (2017) that even in an anechoic environment there is an uncertainty error for every measurement point that can vary from 0.1 dB to 0.5 dB. This uncertainty will impact the calibration of the instrument, increasing the uncertainty levels. To simulate similar conditions a random noise signal with can be added to the magnitude of the simulated radiation patterns. In this work we evaluate the minimum and maximum measurement uncertainties that have been reported to the literature by adding two separate random signals with  $\pm 0.1$  dB and  $\pm 0.5$  dB average in the the simulated patterns. It is worth noting that we assume far field measurements and we do not use the phase of the measured signal. In the case that a near field system is used, then the phase of the measured data will also be taken into account since a Fourier transform is required to obtain the far field data from near field measurements.

Additional to the impact of the measurement uncertainty, filtering strategies of the measured data are explored in this work. Since we have classified the antennas in this work in low and high angular resolution antennas corresponding strategies are explored but applied in either case for further evaluation. Filtering the measured radiation pat-

tern is also based on the fact that the far field function is a smooth function that cannot support spatial harmonics greater than  $\lambda/D$ , where  $D$  is the diameter of the smallest sphere that encloses the antenna. This implies the variations scale with  $\lambda/D$  in the far field measurements, [Balanis \(2005\)](#). The value for the smallest  $\lambda/D$  corresponds to the higher order spatial harmonic that is supported by the structure. This relation will provide the length of the moving filtering window.

The first smoothing filter utilized in this work is a convolution filter with Hamming window, [Antoniou \(2006\)](#) and [Proakis & Manolakis \(2007\)](#). The Hamming window is one of the most commonly used windows as it provides a good trade off between stop band attenuation and pass band transition. We denote the convolution filter with Hamming window as C-H filter. The other smoothing filter utilized in this work is the Savitzky Golay filter, [Luo et al. \(2005\)](#) and [Schafer \(2011\)](#), denoted here as S.G. filter. The basic principle of this filter is that each data point is smoothed by taking into account the average of its neighboring values (linear), however higher order basis sets are possible to be utilized. We have used a 2<sup>nd</sup> order polynomial for the low angular antenna class and a 3<sup>rd</sup> order polynomial for the high angular class in order to be able to follow the pattern peaks with higher accuracy. The motivation for these two filters (C-H and S.G.) stems from their respective behavior, the C-H filter is able to preserve the shape of a low order smooth function hence it is more applicable to the low angular resolution class. In contrast, the S.G. filter with a 3<sup>rd</sup> order polynomial is more suitable for the high angular resolution class as it can better preserve the peak values where the C-H filter always provides an underestimate.

A summary of the results obtained when the proposed piecewise algorithm is used, including the noise and the filtering strategies are tabulated in Table 3 using equation (8) and for a 5<sup>th</sup> order polynomial fit. The data accounted in the table are for the entire bandwidth of observation. It is observed that for the ideal pattern we have a maximum 4.408 mK  $\langle F_{oM}(\hat{n}) \rangle$  for only 8 days of simulated observation data. The impact of the 0.5 dB additive measurement noise impacts more the HERA since the side lobes are uniformly spread whereas the CLDA has high side lobes in the two principal planes. The dipole is the least affected by the measurement noise as expected as it can support only one spatial harmonic and the noise will average out. SKALA is also affected as is visible from the  $\langle F_{oM}(\hat{n}) \rangle$  that is in the order of 0.5 mK due to the rippling in the radiation pattern. The filters perform similarly with some advantage to C-H filter to the low angular class and the S.G. filter to the high angular antenna class but overall the initial values were able to be recovered.

## 6 ON THE ESTIMATION OF THE EOR SIGNAL

To evaluate the proposed method in this work a model of the EoR signal is injected into the foregrounds at every pixel and the simulations are repeated to obtain the antenna temperature using equation (18). The model of the EoR signal used is depicted in Fig. 18. The modeled EoR signal is added to the overall sky temperature according to equation (12).

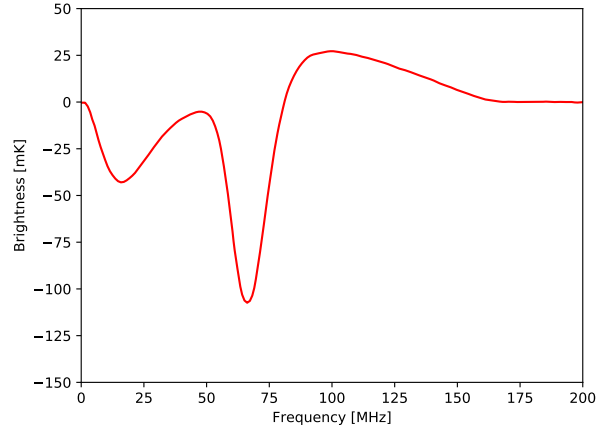


**Figure 18.** EoR signal model.

The realistic dipole and the CLDA proposed in this work are used for the presented results in this section. These two models are representative of the low and high angular resolution antennas. In addition, the two models have inflection points within the band of interest.

$$T_{sky}(\nu, \mathbf{s}) = (T_{Sky\ Model}(\mathbf{s}) - T_{CMB}) \left( \frac{\nu}{\nu_{sky}} \right)^{-\beta} + T_{CMB} + EoR. \quad (18)$$

The largest variation of the signal is expected between 40-100 MHz where the probability of detection is increased and the effort in this part of the work is focused on that region. The antenna temperature is calculated using equations (12) and (18) for the sky model. Following the procedure in this work a logarithmic polynomial fit is performed at the simulated antenna temperature that includes the EoR signal for different polynomial orders. In addition, the simulated antenna temperature containing the EoR signal was also fitted with the polynomial fit according to equation (19) as was suggested in the recent work of [Bowman et al. \(2018\)](#).

$$\hat{T}_{fg}(\nu) = \sum_{n=0}^{m-1} \alpha_n \nu^{n-2.5} \quad (19)$$

The results of this polynomial fitting were similar to the ones obtained to the fitting used in this work and for consistency are not presented here. To obtain the residual EoR signal, the fitted curve is subtracted from the initial simulated antenna temperature. The residuals depicted in Fig. 19 are obtained with 4<sup>th</sup> and 5<sup>th</sup> order polynomial fitting without using the methodology proposed in this work. It is clear that in the case of the CLDA the EoR signal is fitted with the foregrounds and it is not recoverable whereas in the case of the realistic dipole follows the shape of the EoR signal but without the correct level. In Fig. 20 the residual EoR signal is presented for the same case as before but now the proposed methodology is utilized. We observe that the residual closely follows the EoR model. It is worth to note that the concerns have been raised on the foreground polynomial fitting in the work of [Hills et al. \(2018\)](#). An alternative method using maximally smooth functions is presented in [Rao et al. \(2017\)](#).

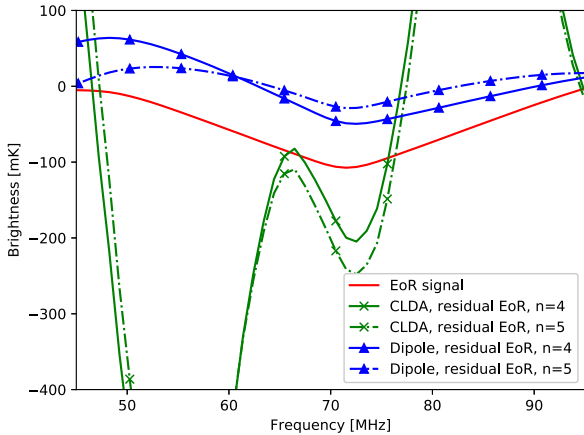


**Figure 19.** Residual EoR signal after the foreground removal with logarithmic polynomial fitting without using the proposed methodology.

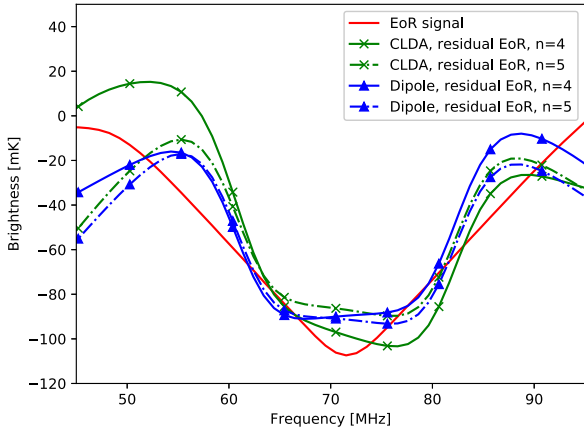


**Figure 20.** Residual EoR signal after the foreground removal using the proposed methodology.

During the analysis in this section the HERA and the SKALA antennas were also used. Based on the gradients presented in Fig. 13 it is observed that within the bandwidth of interest we have the majority of the inflection points. This resulted that the bandwidth intervals between the two inflection points were very small. Based on our analysis the location and the sparsity of the residuals is critical to successfully retrieve the EoR. The CLDA and the simulated dipole have inflection points within the bandwidth of interest but are sparser. This behavior helps us to draw the conclusion that the  $CFoM$  according to equation (16) has to be minimized and any occurring inflection points have to be distributed within the overall bandwidth during the design procedure of the antenna.

## 7 CONCLUSIONS

In this paper we have investigated the implications at the global EoR experiment from the foreground effect as well as selected antenna models that represent different antenna classes. The candidate antennas for the global EoR experi-

ment were divided into low and high angular resolution and their performance was evaluated with the foreground models found in literature and the one proposed in this work. We have found that our proposed foreground model can serve as an empirical lower bound for the detection of the global signal. In addition, it was shown that if a high angular resolution antenna is selected for this experiment the proposed foreground model is able to capture the angular dependency of the spectral index. We have further explored a wideband array design, the CLDA, as a global EoR probe. Though this approach will have practical implementation issues due to the increased complexity, it serves as an excellent reference case for smooth antenna beam patterns.

A general measure, the  $CFoM$  was also introduced in this study as an indicator for the overall antenna chromaticity across the entire frequency of operation. A low  $CFoM$  can also be interpreted that the power spectrum of the antenna beam does not contaminate the global EoR. A general piecewise polynomial fitting algorithm was proposed as an exit strategy for antennas with  $CFoM$ . It was shown that there is a probability of detection of the global signal even with an antenna with high  $CFoM$ . Even though the proposed algorithm was applied only to the antenna directivity in this work it is not limited there and we can apply it to the entire receiver chain and even at the experimental data. This can provide an exit strategy for possible non linearities that are introduced from radical factors such as the antenna efficiency or receiver gain.

We have investigated the impact of measurement uncertainty of the antenna beam patterns. As even in an anechoic environment a  $\pm 0.1$  dB measurement uncertainty is expected this will influence the predicted performance of the instrument. Currently, mainly drone measurements are practical to be performed for such systems due to the size since access to an anechoic chamber can be difficult. For this reason, a  $\pm 0.5$  dB uncertainty was also introduced. Two different filtering strategies of such uncertainties were also evaluated, the Savitzky Golay filter and a convolution filter with Hamming window. The choice of the filters was motivated as the SG filter can follow better the maxima of a function whereas the CV filter the shape hence the one can be applied to high resolution antennas and the other one in the low angular resolution.

Finally, we have investigated the effectiveness of the proposed methodology with realistic simulated data where the EoR signal is injected in the sky model at every pixel. Results using two antennas, the realistic dipole and the CLDA described in this work, and using the proposed methodology were presented. It was shown that we could provide a residual signal resembling the EoR. The gradient of the antenna temperature and the  $CFoM$  could potentially be added as design parameters of the antenna when an experimental set up for such an experiment is prepared.

## ACKNOWLEDGEMENTS

This work was financially supported by The Swedish Governmental Agency for Information Systems (VINNOVA) within the VINN Excellence center, Chase stage IV and ChaseOn through the research project Next Generation Antenna Arrays and integrated Antenna Arrays. This research

was also supported by the Science & Technology Facilities Council (UK) grant: *SKA, ST/M001393/1* and the University of Cambridge, UK. The authors would also like to thank Gianni Bernardi for the useful discussions and Andrew J. Faulkner for revising our manuscript.

## REFERENCES

- Adam R., et al., 2015, *Astron. Astrophys.*, 594, A9. 42 p  
 Antoniou A., 2006, *Digital Signal Processing: Signals, Systems, and Filters*. McGraw Hill  
 Balanis C. A., 2005, *Antenna theory: analysis and design*. Wiley-Interscience  
 Bernardi G., McQuinn M., Greenhill L. J., 2015, *The Astrophysical Journal*, 799, 11  
 Bittner J. M., Loeb A., 2010, *eprint arXiv*, 1006, 5460  
 Bowman J. D., Morales M. F., Hewitt J. N., 2009, *The Astrophysical Journal*, 695, 183  
 Bowman J. D., Rogers A. E., Monsalve R. A., Mozdzen T. J., Mahesh N., 2018, *Nature*, 555, 67  
 Burns J. O., et al., 2012, *Advances in Space Research*, 49, 433  
 CST 2016, Computer Simulation Technology-Microwave Studio CST ® MWS ® 2016  
 Carilli C. L., Furlanetto S., Briggs F., Jarvis M., Rawlings S., Falcke H., 2004, *New Astronomy Reviews*, 48, 1029  
 De Lera Acedo E., et al., 2018, *Experimental Astronomy*, 45, 1  
 DeBoer D. R., et al., 2017a, *PASP*, 129, 045001  
 DeBoer D. R., et al., 2017b, *Publications of the Astronomical Society of the Pacific*, 129, 045001  
 Dillon J. S., et al., 2014, *Physical Review D - Particles, Fields, Gravitation and Cosmology*, 89  
 Fan X., Carilli C. L., Keating B., 2006, *Annu. Rev. Astro. Astrophys.*, 44, 84  
 Furlanetto S. R., 2006, *Monthly Notices of the Royal Astronomical Society*, 371, 867  
 Gnedin N. Y., Shaver P. A., 2004, *The Astrophysical Journal*, 608, 611  
 Haarlem M. P. V., Wise M. W., Gunst A. W., Heald G., McKean J. P., Hessels J. W. T., Bruyn A. G. D., 2013, *Astronomy and Astrophysics*, 556, A2  
 Haslam C. G. T.; Salter C. J. S. H. W. W. E., 1982, *Astronomy and Astrophysics Supplement Series*, 47, 1, 2, 4  
 Hills R., Kulkarni G., Meerburg P. D., Puchwein E., 2018, *arXiv preprint arXiv:1805.01421*  
 Jelić V., Zaroubi S., Labropoulos P., Bernardi G., De Bruyn A. G., Koopmans L. V., 2010, *Monthly Notices of the Royal Astronomical Society*, 409, 1647  
 Kolitsidas C. I., Jonsson B. L. G., Persson P., Stjerman A., 2014, in 2014 Loughborough Antennas and Propagation Conference (LAPC). pp 723–726, doi:10.1109/LAPC.2014.6996497  
 Liu A., Pritchard J. R., Tegmark M., Loeb A., 2013, *Phys. Rev. D*, 87, 043002  
 Luo J., Ying K., Bai J., 2005, *Signal Processing*, 85, 1429  
 Madau P., Meiksin A., Rees M. J., 1997, *The Astrophysical Journal*, 475, 429  
 Matteo T. D., Perna R., Abel T., Rees M. J., 2002, *The Astrophysical Journal*, 564, 576  
 Matteo T. D., Ciardi B., Miniati F., 2004, *Monthly Notices of the Royal Astronomical Society*, 355, 1053  
 McQuinn M., Zahn O., Zaldarriaga M., Hernquist L., Furlanetto S. R., 2006, *The Astrophysical Journal*, 653, 815  
 Mirocha J., Harker G. J. A., Burns J. O., 2013, *The Astrophysical Journal*, 777, 118  
 Monsalve R. A., Rogers A. E. E., Bowman J. D., Mozdzen T. J., 2017a, *The Astrophysical Journal*, 835, 49  
 Monsalve R. A., Rogers A. E. E., Bowman J. D., Mozdzen T. J., 2017b, *The Astrophysical Journal*, 835, 49  
 Morales M. F., Wyithe J. S. B., 2010, *Annual Review of Astronomy and Astrophysics*, 48, 127  
 Morandi A., Barkana R., 2012, *Monthly Notices of the Royal Astronomical Society*, 424, 2551  
 Mozdzen T. J., Bowman J. D., Monsalve R. A., Rogers A. E. E., 2016, *Monthly Notices of the Royal Astronomical Society*, 455, 3890  
 Mozdzen T. J., Bowman J. D., Monsalve R. A., Rogers A. E. E., 2017, *Monthly Notices of the Royal Astronomical Society*, 464, 4995  
 Neben A. R., et al., 2016, *The Astrophysical Journal*, 820, 44  
 Parsons A. R., et al., 2010, *The Astronomical Journal*, 139, 1468  
 Patra N., Subrahmanyam R., Raghunathan A., Udaya Shankar N., 2013, *Experimental Astronomy*, 36, 319  
 Patra N., Subrahmanyam R., Sethi S., Shankar N. U., Raghunathan A., 2015, *The Astrophysical Journal*, 801, 138  
 Pivnenko S., et al., 2009, *IEEE Transactions on Antennas and Propagation*, 57, 1863  
 Plice L., Galal K., Burns J. O., 2017, preprint, ([arXiv:1702.00286](https://arxiv.org/abs/1702.00286))  
 Price D. C., et al., 2017, preprint, ([arXiv:1709.09313](https://arxiv.org/abs/1709.09313))  
 Pritchard J. R., Loeb A., 2008, *Physical Review D*, 78, 103511  
 Pritchard J. R., Loeb A., 2010a, *Phys. Rev. D*, 82, 023006  
 Pritchard J. R., Loeb A., 2010b, *Physical Review D - Particles, Fields, Gravitation and Cosmology*, 82  
 Proakis J., Manolakis D., 2007, *Digital Signal Processing*. Pearson  
 Pupillo G., et al., 2015, *Experimental Astronomy*, 39, 405  
 Rao M. S., Subrahmanyam R., Shankar N. U., Chluba J., 2017, *The Astrophysical Journal*, 840, 33  
 Remazeilles M., Dickinson C., Banday A. J., Bigot-Sazy M.-A., Ghosh T., 2015, *Monthly Notices of the Royal Astronomical Society*, 451, 4311  
 Rogers A. E. E., Bowman J. D., 2008, *The Astronomical Journal*, p. 8  
 Saporetti M. A., Foged L., Castaner M. S., Pivnenko S., Cornelius R., Heberling D., 2017, *IEEE Antennas and Propagation Magazine*, 59, 108  
 Schafer R. W., 2011, *IEEE Signal Processing Magazine*, 28, 111  
 Sethi S. K., 2005, *Monthly Notices of the Royal Astronomical Society*, 363, 818  
 Shaver P. A., Windhorst R. A., Madau P., de Bruyn A. G., 1999, [arXiv:astro-ph/9901320v1](https://arxiv.org/abs/astro-ph/9901320v1), 390, 1  
 Sokolowski M., et al., 2015, *Publications of the Astronomical Society of Australia*, 32, e004  
 Wang X., Hu W., 2006, *The Astrophysical Journal*, 643, 585  
 Warnick K. F., Ivashina M. V., Maaskant R., Woestenburg B., 2010, *IEEE Transactions on Antennas and Propagation*, 58, 2121  
 Yang M., Yin X., Chen Z. N., Rong Y., Qian H., 2016, *IEEE Antennas and Wireless Propagation Letters*, 15, 658  
 Zaldarriaga M., Furlanetto S. R., Hernquist L., 2004, *The Astrophysical Journal*, 608, 622  
 de Lera Acedo E., Razavi-Ghods N., Troop N., Drought N., Faulkner A. J., 2015, *Experimental Astronomy*, 39, 567  
 de Lera Acedo E., et al., 2017, *Monthly Notices of the Royal Astronomical Society*, 469, 2662  
 de Oliveira-Costa A., Tegmark M., Gaensler B. M., Jonas J., Landecker T. L., Reich P., 2008, *Monthly Notices of the Royal Astronomical Society*, 388, 247  
 van Weeren R. J., et al., 2016, *The Astrophysical Journal Supplement Series*, 223, 2

This paper has been typeset from a TeX/LaTeX file prepared by the author.